ORIGINAL PAPER

Transition control of the blasius boundary layer using linear robust control theory

Christopher J. Damaren[1]

Abstract

The paper considers control system design for linearized three-dimensional perturbations about a nominal laminar boundary layer over a flat plate (the Blasius profile). The objective is prevention of the laminar to turbulent transition using appropriate inputs, outputs, and feedback controllers. They are synthesized with a view to reducing transient energy growth, a known precursor to important transition scenarios. The linearized Navier–Stokes equations are reduced to the Orr–Sommerfeld and Squire equations with wall-normal velocity actuation entering through the boundary conditions on the wall. The sensor output is taken to be the wall-normal derivative of the wall-normal vorticity measured on the plate. Several multivariable output controllers are examined, including simple constant gain output feedback, loop transfer recovery, and H_∞ loop shaping. Reduced order compensators are developed using balanced truncation and analyzed for robustness using the gap metric between reduced order models and full order models. It is demonstrated that the level of minimum transient energy growth that can be achieved is similar for these diverse controller methodologies but falls short of that which can be achieved using optimal state feedback.

1 Introduction

It is well known that the drag force on a body immersed in an unseparated flow strongly depends on the behavior of the boundary layer. In particular, laminar boundary layers produce less drag than turbulent ones. Hence, prevention of transition between the two flow regimes from occurring is an important problem. Transition has historically been studied by linearizing the Navier–Stokes equations about a nominal velocity profile consisting of a baseline laminar flow and addressing the stability of small perturbations [1, 2]. This profile has typically been taken to be the two-dimensional Blasius solution [3] for boundary layer flows over a flat plate. Using the two-dimensional spatial Fourier transform with the linearized equations, one arrives at the Orr–Sommerfeld equation describing the wall-normal velocity component and the Squire equation describing the wall-normal vorticity component. The two equations are coupled when the span-

wise wavenumber is nonzero. Transition can be studied by determining the eigenvalues of the Orr–Sommerfeld/Squire model governing the perturbations [1]. Under this linear scenario, transition corresponds to an eigenvalue crossing into the right-half of the complex plane creating Tollmien–Schlichting waves.

Experimentalists have shown that transition typically occurs at Reynolds numbers (based on distance along the plate) that are smaller than those predicted by linear eigenvalue theory [1]. It is thought that large transient growth in the flow perturbations can trigger transition via nonlinear mechanisms before the linear instability mechanism occurs [2]. Transient growth in the Blasius boundary layer was studied by Butler and Farrell [4], who noted that at some Reynolds numbers, the worst case transient growth occurred at streamwise wavenumbers that were zero and nonzero spanwise wavenumbers.

Both stabilization and suppression of transient growth have been studied using linear state-state models based on the Orr–Sommerfeld/Squire system to design feedback controllers [5]. Much of this work has emphasized plane Poiseuille flow [6, 7] and the Blasius boundary layer [8, 9]. The Poiseuille flow corresponds to the fully-developed flow

✉ Christopher J. Damaren
 chris.damaren@utoronto.ca

[1] Institute for Aerospace Studies, University of Toronto, 4925 Dufferin Street, Toronto, ON M3H 5T6, Canada

in a channel between two parallel infinite plates and the Blasius boundary layer is the two-dimensional laminar flow over a semi-infinite flat plate. This paper will concentrate on the latter case.

The choice of sensors and actuators and their locations has a profound effect on the achievable stability, performance, and robustness of a feedback strategy. Sensor and actuator location has been considered by [6] in the Poiseuille case and [9] in the Blasius case. A very useful paradigm for robust feedback controller design is passivity-based control. A companion paper [10] was devoted to determining a sensor/actuator combination that led to a passive input–output map. The motivation for this was the passivity theorem [11] which states that the negative feedback interconnection of a passive system and a strictly passive system (with finite gain) is L_2-stable, that is, L_2 (finite energy) inputs produce L_2 (finite energy) outputs. In earlier work [12], we studied the passivity property in the context of the Orr–Sommerfeld equation with actuation inputs implemented as wall-normal velocity. A dual output (based on energy analysis) was shown to be the second spatial derivative (normal direction) of the streamwise velocity perturbation at the wall. Other authors [13, 14] have used passivity ideas in the stabilization of a Poiseuille flow where dynamic linear controller designs were employed to render the closed-loop system to be passive.

In our previous work [10], the analysis was carried out in three spatial dimensions using both the Orr–Sommerfeld and Squire equations. Passivity of the system mapping wall-normal velocity inputs to three spatial derivatives (in the wall-normal direction) of the wall-normal velocity as the output was shown to be passive when the streamwise wavenumber is zero. This is precisely the case corresponding to largest transient growth at certain Reynolds numbers as identified in [4]. Unfortunately, this passive output does not render the wall-normal vorticity states observable. For this reason, we introduce an alternative output in this paper, namely one spatial derivative (wall-normal direction) of the wall-normal vorticity evaluated on the wall. This is obtainable from shear-stress measurements on the wall.

Spatial discretization of the Orr–Sommerfeld and Squire equations will be accomplished using Hermite cubic finite elements to describe the wall-normal velocity and vorticity components. This approach was originally used for the Orr–Sommerfeld equation with Poiseuille flows in [15]. Our controller studies examine the following control system design paradigms: state feedback using the linear quadratic regulator (LQR), output feedback designs based on a single scalar feedback gain, linear quadratic gaussian/loop transfer recovery (LQG/LTR), and H_∞ loop shaping, and reduced order designs based on model order reduction using balanced truncation. Robustness of this latter control solution is analyzed using the gap metric [16, 17]. The second of our major contributions is a demonstration that the level of minimum

transient energy growth that can be achieved is similar for these diverse controller methodologies but falls short of that which can be achieved using optimal state feedback based on LQR theory. A recent paper by Jones et al. [18] examined H_∞ loop-shaping designs for Poiseuille flow.

Some of the more recent works on the control of boundary layer transition are [19–24]. Gibeau and Ghaemi [19] studied actuation for boundary layer control using wall normal surface deformation. Methel et al. [20] looked at the impact of steps and gaps on control using wall normal suction. Li and Chen [21] examined feedback control of Tollmien–Schlichting waves using a simple PID controller. In [22], Gluzman and Gayme developed an input–output framework for examining the impact of different actuation and sensing on boundary layer control. O'Connor et al. [24] studied the optimization of streamwise-varying wall-normal blowing for control of turbulent boundary layers. Although our emphasis is on the flat-plate boundary layer, the ultimate application is to aircraft lifting surfaces whose state-of-the-art is described by Svorcan, Wang, and Griffin [23]. It is important to note that while the papers [8, 9] represent some of the most recent work on transition control of the Blasius boundary layer using feedback, they are two-dimensional studies whereas the current work considers three-dimensional flow perturbations.

The paper is organized as follows. Section 2 examines controller design methods for multivariable linear time-invariant (LTI) systems. Section 3 develops the Orr–Sommerfeld and Squire equations and the output described above using the wall-normal vorticity is shown to be realizable by shear stress measurements at the wall. Section 4 presents the spatial discretization of the Orr–Sommerfeld/Squire equation based on the finite element method. Numerical results are presented for the case considered by Butler and Farrell [4], namely a Reynolds number (based on displacement thickness) of 1000, a spanwise wavenumber of 0.65, and a streamwise wavenumber of zero. Emphasis is placed on computing the maximum transient energy growth for LQR state feedback as well as output feedback controllers using the alternative output based on sensing the wall-normal derivative of the wall-normal vorticity. These latter cases include simple constant gain output feedback, LQG/LTR, H_∞ loop shaping, and reduced order designs based on model order reduction of the plant using balanced truncation. Robustness of this latter control solution is analyzed using the gap metric. Section 5 presents some concluding remarks.

2 Feedback controller design

2.1 Feedback design

The feedback system shown in Fig. 1 is considered where $d_1(t)$, $d_2(t)$, $m_1(t)$, and $m_2(t)$ are functions of time t.
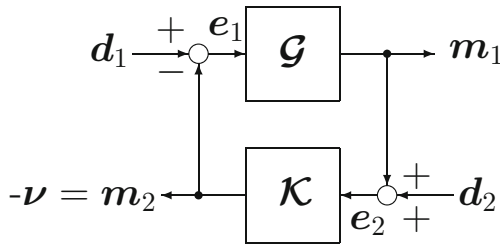
Fig. 1 Feedback system

The L_2-space consists of those functions m for which the L_2-norm satisfies $||m||_2 \triangleq \sqrt{\int_0^\infty m^\mathsf{T}(t)m(t)\,dt} < \infty$ (the symbol $(\ )^\mathsf{T}$ denotes the matrix transpose and $(\ )^\mathsf{H}$ denotes the complex-conjugate transpose). The extended L_2-space, L_{2e}, consists of those functions for which $||m||_{2T} \triangleq \sqrt{\int_0^T m^\mathsf{T}(t)m(t)\,dt} < \infty, 0 \leq T < \infty$. Note that $L_2 \subset L_{2e}$. Consider the system to be controlled $m_1(t) = (\mathcal{G}e_1)(t)$ where the operator $\mathcal{G} : L_{2e} \to L_{2e}$ (possibly nonlinear and time-varying) maps the input $e_1 \in L_{2e}$ into the output $m_1 \in L_{2e}$. The gain of $\mathcal{G}$ is the induced norm on L_2 and is defined to be $||\mathcal{G}|| = \sup_{0 \neq e_1 \in L_2} ||\mathcal{G}e_1||_2/||e_1||_2$.

In the case where $\mathcal{G}$ is linear time-invariant (LTI) (and finite dimensional), it can be described using the standard state-space model

$$\dot{x}(t) = Ax(t) + Be_1(t) \tag{1}$$

$$m_1(t) = Cx(t) + De(t) \tag{2}$$

where $(\dot{\ })$ denotes the time derivative. This system can be described using transfer functions: $m_1(s) = G(s)e_1(s)$ where $m_1(s)$ denotes the Laplace transform of $m_1(t)$ (a common abuse of notation) and $G(s)$ is the system transfer (function) matrix. The quantity s denotes the complex-valued Laplace transform variable and $\mathrm{i} = \sqrt{-1}$. Note that

$$G(s) = \left[\begin{array}{c|c} A & B \\ \hline C & D \end{array}\right] \triangleq C(sI - A)^{-1}B + D \tag{3}$$

is the transfer matrix corresponding to the state-space model in Eqs. (1) and (2). Here, I is the identity matrix of appropriate dimension. If the system is controllable and observable, then L_2-stability of $\mathcal{G}$ ($e_1 \in L_2$ implies that $m_1 = \mathcal{G}e_1 \in L_2$) corresponds to the matrix A having eigenvalues with negative real parts. For stable LTI systems, the gain can be shown [25] to be $||\mathcal{G}|| = ||G(s)||_\infty = \sup_{\omega \in \mathcal{R}} \bar{\sigma}[G(\mathrm{i}\omega)]$ where $\bar{\sigma}$ denote the largest singular value. The system $\mathcal{K}$ in Fig. 1 represents the controller which we seek to design. A minimal requirement would be L_2-stability of the closed-loop system, i.e, $d_1, d_2 \in L_2$ implies that $e_1, e_2, m_1, m_2 \in L_2$.

2.2 LTI feedback controller design

Consider the case where $\mathcal{G}$ and $\mathcal{K}$ correspond to LTI systems with transfer matrices $G(s) = C(sI - A)^{-1}B + D$ and $K(s)$, respectively. Considering the closed-loop system depicted in Fig. 1, we write the closed-loop transfer matrix mapping (d_1, d_2) to (e_1, m_1) by

$$[G(s), K(s)] \triangleq \begin{bmatrix} I \\ G(s) \end{bmatrix} [I + K(s)G(s)]^{-1}[I \quad -K(s)] \tag{4}$$

(We will occasionally omit the argument s of transfer matrices.) We will also require the loop shape transfer function $L(s) = K(s)G(s)$ and make special reference to the (input) sensitivity function $S(s) = [I + K(s)G(s)]^{-1}$ which is the transfer matrix from d_1 to e_1 when $d_2 = 0$. The matrix $H(s) = G(s)S(s)$ is the transfer matrix from d_1 to m_1 when $d_2 = 0$. It is easily shown that if a square plant $G(s)$ is perturbed to $G(s) + \Delta G(s)$, then for small perturbations, the corresponding small change in $H(s)$, $\Delta H(s)$ satisfies $[\Delta H(s)H^{-1}(s)][\Delta G(s)G^{-1}(s)]^{-1} = S(s)$.

In the case of a static compensator, $m_2 = -v = \bar{K}e_2$ where $\bar{K}$ is a constant matrix,

$$[G(s), K(s)] = \left[\begin{array}{c|c} \begin{array}{cc} A - B\Gamma_{KD}\bar{K}C \\ -\Gamma_{KD}\bar{K}C \\ \Gamma_{DK}C \end{array} & \begin{array}{ccc} B\Gamma_{KD} & -B\Gamma_{KD}\bar{K} \\ \Gamma_{KD} & -\Gamma_{KD}\bar{K} \\ \Gamma_{DK}D & -\Gamma_{DK}D\bar{K} \end{array} \end{array}\right],$$
$$\Gamma_{KD} = [I + \bar{K}D]^{-1}$$
$$\Gamma_{DK} = [I + D\bar{K}]^{-1} \tag{5}$$

Considering strictly proper dynamic compensators of the form

$$K(s) = K_c(sI - A_c)^{-1}K_e \tag{6}$$

leads to

$$[G(s), K(s)] = \left[\begin{array}{cc|cc} A & -BK_c & B & 0 \\ K_eC & A_c - K_eDK_c & K_eD & K_e \\ \hline 0 & -K_c & I & 0 \\ C & -DK_c & D & 0 \end{array}\right] \tag{7}$$

The upper left 2×2 partition (i.e., the closed-loop system matrix) will be denoted by $\bar{A}$ with corresponding initial conditions $\bar{x}(0) = \mathrm{col}\{x(0), 0\}$ (i.e., quiescent initial condition for the controller states). In the case of a static compensator, $\bar{A} = A - B\Gamma_{KD}\bar{K}C$ which collapses to A in the open-loop case.

2.3 Measuring transient growth

Considering the system in Eq. (7) with the exogenous inputs taken to be $d_1 = d_2 = 0$ with nonzero initial conditions $x(0)$

yields

$$x(t) = T(t)x(0), \quad T(t) = [I \ \ 0] \exp(\bar{A}t)[I \ \ 0]^\mathsf{T} \quad (8)$$

It is assumed that the energy of the system is calculated using the quadratic form

$$E(t) = \frac{1}{2} x^\mathsf{T}(t) Q x(t) \quad (9)$$

where $Q = Q^\mathsf{T} > 0$. The largest transient energy growth [26] can be calculated by determining the initial conditions $x(0)$ to maximize the quantity

$$J = \sup_{T \geq 0} \sup_{x(0)} \left\{ \frac{E(T)}{E(0)} \right\} \quad (10)$$

$$= \sup_{T \geq 0} \sup_{x(0)} \left\{ \frac{x^\mathsf{T}(0) T^\mathsf{T}(T) Q T(T) x(0)}{x^\mathsf{T}(0) Q x(0)} \right\}. \quad (11)$$

This leads to a generalized symmetric eigenproblem ($\lambda Q \bar{x} = T^\mathsf{T}(T) Q T(T) \bar{x}$) nested within a search over $T \geq 0$. The maximum eigenvalue λ for given T yields the maximum energy ratio $E(T)/E(0)$ and the eigenvector $\bar{x}$ corresponding to it yields the optimal initial condition. The quantity $E(T)/E(0)$ is then optimized with respect to T using a direct search to determine J.

2.4 The linear quadratic regulator (LQR)

Consider the plant model $\dot{x} = Ax + Bv$ (i.e., $d_1 = d_2 = 0$). In an effort to minimize J our baseline controller will be chosen to minimize the quadratic performance index

$$J_{LQR} = \frac{1}{2} \int_0^\infty \left(x^\mathsf{T}(t) Q x(t) + v^\mathsf{T}(t) R v(t) \right) dt \quad (12)$$

where the weighting matrices are chosen such that Q is symmetric and non-negative definite and R is selected to be symmetric and positive definite. This is the well-known linear quadratic regulator (LQR) which has the feedback solution $v(t) = -K_{LQR}x(t)$ with feedback gain $K_{LQR} = R^{-1}B^\mathsf{T}P_{LQR}$. The matrix P_{LQR} is the solution of the algebraic Riccati equation $P_{LQR}A + A^\mathsf{T}P_{LQR} - P_{LQR}BR^{-1}B^\mathsf{T}P_{LQR} + Q = 0$. This equation has a unique positive-semidefinite solution if (A, B) is stabilizable. In this case, the transient energy growth can be calculated with $\bar{A} = A - BK_{LQR}$. Since this is state feedback, we have $C = I$ and $D = 0$, so that $L_{LQR}(s) = K_{LQR}(sI - A)^{-1}B$ with sensitivity function $S_{LQR}(s) = [I + L_{LQR}(s)]^{-1}$. It would be useful to have a dynamic compensator using output feedback which could in some sense "recover" the LQR performance. This is done in the next section using the Linear

Quadratic Gaussian (LQG)/ Loop Transfer Recovery (LTR) methodology.

2.5 Loop transfer recovery

The LQG/LTR controller [27] considered here (as well as the H_∞ loop-shaping controllers considered in the next section) has the form:

$$K(s) = \left[\begin{array}{c|c} A - BK_c - K_eC & K_e \\ \hline K_c & 0 \end{array} \right] \quad (13)$$

which is an observer-based compensator. It will be assumed for Sects. 2.5 and 2.6 that the plant is strictly proper ($D = 0$). In the loop transfer recovery approach, the following selections are made: $K_c = K_{LQR}$ and $K_e = P_eC^\mathsf{T}$ where

$$P_eA^\mathsf{T} + AP_e - P_eC^\mathsf{T}CP_e + q_0BB^\mathsf{T} = 0$$

and q_0 is a design parameter. If (A, B) is controllable and (C, A) is observable then $L(s) \rightarrow L_{LQR}(s)$ and then $S(s) \rightarrow S_{LQR}(s)$ (pointwise) as $q_0 \rightarrow \infty$. An interesting question that arises is how does the transient growth measure, J, behave relative to the LQR case as $q_0 \rightarrow \infty$?

2.6 H_∞ design

Clearly, a useful approach to controller design would minimize the impact of d_1 and d_2 on e_1 and m_1, or in other words, maximize $b_{G,K} \triangleq ||[G(s), K(s)]||_\infty^{-1}$. A suboptimal controller design which yields $||[G(s), K(s)]||_\infty < \gamma$ for prescribed $\gamma > 0$ is given by [17, 28] $K_c = B^\mathsf{T}X$ where

$$XA + A^\mathsf{T}X - XBB^\mathsf{T}X + C^\mathsf{T}C = 0 \quad (14)$$

The controller input matrix or "estimation gain" is given by $K_e = -\gamma^2 W_1^{-\mathsf{T}} ZC^\mathsf{T}$ where $W_1 = I + (XZ - \gamma^2 I)$ and

$$ZA^\mathsf{T} + AZ - ZC^\mathsf{T}CZ + BB^\mathsf{T} = 0 \quad (15)$$

For this to be valid, γ must be selected to be greater than the optimal value $\gamma_{\min} = \sqrt{1 + \lambda_{\max}(ZX)} = b_{\mathrm{opt}}^{-1}(\mathcal{G})$ where

$$b_{\mathrm{opt}}(\mathcal{G}) = \sup_{\mathrm{stab}\, K} b_{G,K} \quad (16)$$

This controller has an interesting robustness interpretation.

2.7 The gap metric and robustness

Consider a nominal system $\mathcal{G}_1$ and a perturbed system $\mathcal{G}_2$. We are interested in knowing, under what conditions, a controller that stabilizes $\mathcal{G}_1$ will also stabilize $\mathcal{G}_2$. This requires a metric that can evaluate the distance between $\mathcal{G}_1$ and $\mathcal{G}_2$

in some sense. A useful possibility is the gap metric [16], denoted by $\delta_g(\mathcal{G}_1, \mathcal{G}_2)$.

The domain of an operator $\mathcal{G}$ is defined here as $\mathcal{D}(\mathcal{G}) = \{e \in L_2 \mid \mathcal{G}e \in L_2\}$. The graph of $\mathcal{G}$ is the collection of pairs $\{e, \mathcal{G}e\}$ with $e \in \mathcal{D}(\mathcal{G})$. Now, consider two LTI systems represented by the operators $\mathcal{G}_1$ and $\mathcal{G}_2$ with corresponding transfer matrices $G_1(s)$ and $G_2(s)$. The gap metric describing the distance between $\mathcal{G}_1$ and $\mathcal{G}_2$ is defined as

$$\delta_g = \max\{\vec{\delta}(\mathcal{G}_1, \mathcal{G}_2), \vec{\delta}(\mathcal{G}_2, \mathcal{G}_1)\}$$

where the directed gap is defined as

$$\vec{\delta}(\mathcal{G}_1, \mathcal{G}_2) = \sup_{0 \neq e_1 \in \mathcal{D}(\mathcal{G}_1)} \inf_{e_2 \in \mathcal{D}(\mathcal{G}_2)}$$
$$\times \frac{(\|e_2 - e_1\|_2^2 + \|\mathcal{G}_2 e_2 - \mathcal{G}_1 e_1\|_2^2)^{1/2}}{(\|e_1\|_2^2 + \|\mathcal{G}_1 e_1\|_2^2)^{1/2}}$$

This time-domain calculation is not useful in practice but there is a frequency-domain calculation that is.

It is known that a real rational transfer matrix admits the right normalized coprime factorization [29]

$$G(s) = N(s)M^{-1}(s)$$

where $N(s)$ and $M(s)$ are real-rational stable transfer functions (i.e., they are real rational and are elements of H_∞ and are normalized such that $M^\mathsf{T}(-s)M(s) + N^\mathsf{T}(-s)N(s) = I$. Assuming $G_i(s) = N_i(s)M_i^{-1}(s)$, $i = 1, 2$, are normalized right coprime factorizations, the directed gap can be calculated using [30]

$$\vec{\delta}(\mathcal{G}_1, \mathcal{G}_2) = \inf_{Q(s) \in H_\infty} \left\| \begin{pmatrix} M_1(s) \\ N_1(s) \end{pmatrix} - \begin{pmatrix} M_2(s) \\ N_2(s) \end{pmatrix} Q(s) \right\|_\infty$$

This is a calculation for which numerical procedures exist. In our work, we employ the procedure developed in [31] and the required normalized right coprime factorizations are calculated using [29].

As noted in [16] and [17], $\delta(\mathcal{G}_1, \mathcal{G}_2)$ is a metric and $0 \leq \delta(\mathcal{G}_1, \mathcal{G}_2) \leq 1$. To gain some insight into the behavior of the gap metric, consider the following example from [17]. If $G_1(s) = k_1/(s + 1)$ and $G_2(s) = k_2/(s + 1)$, then

$$\delta(\mathcal{G}_1, \mathcal{G}_2) = \begin{cases} \frac{|k_1 - k_2|}{|k_1| + |k_2|}, & |k_1 k_2| > 1 \\ \frac{|k_1 - k_2|}{\sqrt{(1 + k_1^2)(1 + k_2^2)}}, & |k_1 k_2| \leq 1. \end{cases}$$

The key robustness theorem involving the gap metric is the following [17]: The system $[G_1(s), K(s)]$ is stable for all $G_1(s)$ with $\delta_g(\mathcal{G}_1, \mathcal{G}) < b$ if and only if $[G(s), K(s)]$ is stable and $b < b_{G,K}$. Hence, optimal robustness in the gap metric is obtained by employing a controller K that maximizes $b_{G,K}(\mathcal{G})$. In our numerical results, we will employ this
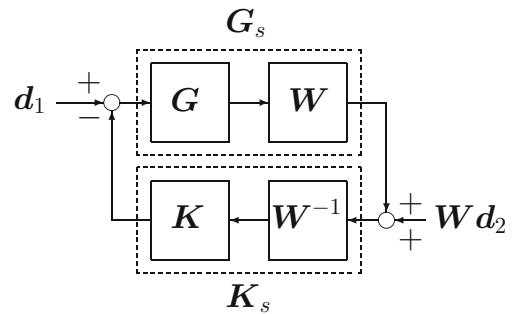

Fig. 2 Feedback system with loop shaping

theorem to gauge the robustness of reduced order controller designs based on reduced order models of $\mathcal{G}$.

2.8 H_∞ loop shaping

The controller with optimal robustness described in Sect. 2.6 may not perform very well. To remedy this, one can design the above controller for a loop-shaped plant [32]. In our work we consider the shaped plant $G_s(s) = WG(s)$ where $W = WI$, $W > 0$. The stability of the system in Fig. 1 (LTI case) is the same as the loop-transformed feedback system shown in Fig. 2. The idea is to design the feedback compensator $K_s(s) = K(s)W^{-1}$ according to Sect. 2.6 for the shaped plant $G_s(s)$ which can be realized by simply multiplying the matrix C by W. The actual controller $K(s)$ can be obtained from $K_s(s)$ by multiplying the matrix K_e by W.

2.9 Model order reduction

The controller designs presented above have assumed a full-order model. Next, a controller with a reduced number of states is developed by employing a controller design using a reduced order model. In this paper, we shall employ a two-step method of model order reduction. First, assume that the system $G(s)$ has been transformed to modal form. Assuming $D = 0$ and the eigenvalues of A, λ_i, are distinct, the modal system is given by

$$G(s) = \left[\begin{array}{cccc|c} \lambda_1 & 0 & \cdots & 0 & \hat{b}_1^\mathsf{H} \\ 0 & \lambda_2 & \cdots & 0 & \hat{b}_2^\mathsf{H} \\ \vdots & \vdots & \ddots & \vdots & \vdots \\ 0 & 0 & \cdots & \lambda_n & \hat{b}_n^\mathsf{H} \\ \hline \hat{c}_1 & \hat{c}_2 & \cdots & \hat{c}_n & 0 \end{array} \right] \tag{17}$$

Assuming distinct eigenvalues, the conditions for modal controllability and modal observability are $\|\hat{b}_\alpha\| > 0$ and $\|\hat{c}_\alpha\| > 0$. Since the balanced truncation approach given below assumes controllability and observability, we begin by obtaining an intermediate-sized model which uses

modal coordinates and the first 100 modes with the largest values of $||\hat{\boldsymbol{b}}_\alpha|| \cdot ||\hat{\boldsymbol{c}}_\alpha||$. Hence, they are the most controllable/observable as measured by the product of the modal controllability and observability norms.

For the intermediate-size model (we abuse notation and assume this system is $\boldsymbol{G}(s) = \boldsymbol{C}(s\boldsymbol{I} - \boldsymbol{A})^{-1}\boldsymbol{B}$) consider the Lyapunov equations

$$\boldsymbol{P}\boldsymbol{A}^\mathsf{T} + \boldsymbol{A}\boldsymbol{P} + \boldsymbol{B}\boldsymbol{B}^\mathsf{T} = \boldsymbol{0} \tag{18}$$

$$\boldsymbol{Q}\boldsymbol{A} + \boldsymbol{A}^\mathsf{T}\boldsymbol{P} + \boldsymbol{C}^\mathsf{T}\boldsymbol{C} = \boldsymbol{0} \tag{19}$$

where $\boldsymbol{P}$ and $\boldsymbol{Q}$ are the controllability and observability gramians, respectively. A state realization in which $\boldsymbol{P}$ and $\boldsymbol{Q}$ are diagonal and equal is called a balanced realization [33]. In such a representation, the diagonal entries are called the Hankel singular values, $\sigma_i = \sqrt{\lambda_i\{\boldsymbol{P}\boldsymbol{Q}\}}$, which are invariants under state transformations. From [34], there exists a state transformation $\hat{x} = \boldsymbol{T}x$ resulting in a new state-space model with realization

$$\boldsymbol{G}(s) = \left[\begin{array}{cc|c} \hat{\boldsymbol{A}}_{11} & \hat{\boldsymbol{A}}_{12} & \hat{\boldsymbol{B}}_1 \\ \hat{\boldsymbol{A}}_{21} & \hat{\boldsymbol{A}}_{22} & \hat{\boldsymbol{B}}_2 \\ \hline \hat{\boldsymbol{C}}_1 & \hat{\boldsymbol{C}}_2 & \boldsymbol{0} \end{array}\right] \tag{20}$$

where

$$\boldsymbol{P} = \boldsymbol{Q} = \begin{bmatrix} \boldsymbol{\Sigma}_1 & \boldsymbol{0} \\ \boldsymbol{0} & \boldsymbol{\Sigma}_2 \end{bmatrix} \tag{21}$$

where $\boldsymbol{\Sigma}_1 = \mathrm{diag}\{\sigma_1, \ldots, \sigma_r\}$ and $\boldsymbol{\Sigma}_2 = \mathrm{diag}\{\sigma_{r+1}, \ldots, \sigma_N\}$. It is assumed that $\sigma_1 \geq \sigma_2 \geq \cdots \sigma_r > \sigma_{r+1} \geq \cdots \geq \sigma_N$. A reduced order model of order r is given by $\boldsymbol{G}_r = \hat{\boldsymbol{C}}_1(s\boldsymbol{I} - \hat{\boldsymbol{A}}_{11})^{-1}\hat{\boldsymbol{B}}_1$ with error bound

$$||\boldsymbol{G}_r(s) - \boldsymbol{G}(s)||_\infty \leq \Gamma_r \overset{\Delta}{=} 2(\sigma_{r+1} + \ldots \sigma_N) \tag{22}$$

In computing the upper bound, Hankel singular values with a multiplicity greater than one are only included once in the summation. Based on the above results using the gap metric, if $\delta_g(\mathcal{G}_r, \mathcal{G}) < b_{G_r, K_r} = ||[\boldsymbol{G}_r(s), \boldsymbol{K}_r(s)]||_\infty^{-1}$, then a stabilizing controller $\boldsymbol{K}_r(s)$ for the reduced order model $\boldsymbol{G}_r(s)$ will also stabilize the full-order model $\boldsymbol{G}(s)$.

3 Dynamical model based on the Orr–Sommerfeld/Squire equations

3.1 Blasius boundary layer

Let us consider a three-dimensional boundary layer flow field occupying the region $(x, y, z) \in [0, \infty] \times [0, b] \times [-\infty, \infty]$ with a base parallel laminar flow $(U(y), 0, 0)$ and associated

pressure field $P(x, y, z, t)$. The Blasius boundary layer flow [3] is depicted in Fig. 3. Although $b \to \infty$, a finite computational boundary for b will be employed as discussed below. The true boundary layer profile is known to be nonparallel $((U, V, 0), V \neq 0)$, but we shall adopt the approximation $V = 0$ and take $U(y)$ to be the Blasius solution: $U(y) = \mathrm{d}f(\eta)/\mathrm{d}\eta$ (this has been nondimensionalized using the free-stream velocity U_0) where $\eta = y_d\sqrt{\rho U_0/(\mu x_d)}$ (x_d, y_d, and z_d refer to dimensional coordinates) and $f(\eta)$ is the solution of $2\mathrm{d}^3 f/\mathrm{d}\eta^3 + (\mathrm{d}^2 f/\mathrm{d}\eta^2)f = 0$ with $\mathrm{d}f(0)/\mathrm{d}\eta = f(0) = 0$ and $\mathrm{d}^2 f(0)/\mathrm{d}\eta^2 = 0.33205733622$ which yields the correct asymptotic boundary condition $\mathrm{d}f(\eta)/\mathrm{d}\eta = 1$ as $\eta \to \infty$.

A suitable nondimensionalization for the spatial coordinates can be obtained using the displacement thickness $H = \delta^* = 1.7207876573\sqrt{\mu x_d/(\rho U_0)}$ where the free-stream velocity is U_0. The local Reynolds number will be denoted by $Re = \rho U_0 \delta^*/\mu$ where ρ is the fluid density and μ is the absolute viscosity. The displacement thickness δ^* will nondimensionalize length and U_0 will nondimensionalize velocity. In our numerical work, we will use a finite computational domain with $b = 24\sqrt{\mu x_d/(\rho U_0)}/H$ (dimensionless) and at this boundary an inviscid asymptotic solution will be imposed.

3.2 Orr–Sommerfeld/Squire equations

Assuming small perturbations $u(x, y, z, t)$, $v(x, y, z, t)$, $w(x, y, z, t)$, and $p(x, y, z, t)$ about the Blasius flow, the linearized incompressible Navier–Stokes equations [1] are

$$\frac{\partial u}{\partial x} + \frac{\partial v}{\partial y} + \frac{\partial w}{\partial z} = 0 \tag{23}$$

$$\frac{\partial u}{\partial t} + U\frac{\partial u}{\partial x} + U'v = -\frac{\partial p}{\partial x} + \frac{1}{Re}\boldsymbol{\nabla}^2 u \tag{24}$$

$$\frac{\partial v}{\partial t} + U\frac{\partial v}{\partial x} = -\frac{\partial p}{\partial y} + \frac{1}{Re}\boldsymbol{\nabla}^2 v \tag{25}$$

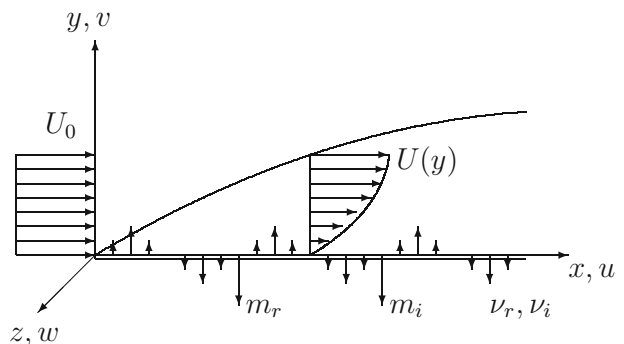$$\frac{\partial w}{\partial t} + U\frac{\partial w}{\partial x} = -\frac{\partial p}{\partial z} + \frac{1}{Re}\boldsymbol{\nabla}^2 w \tag{26}$$

Fig. 3 Blasius boundary layer

where $U'(y) = \mathrm{d}U(y)/\mathrm{d}y$ and $\nabla^2 = \partial^2/\partial x^2 + \partial^2/\partial y^2 + \partial^2/\partial z^2$. It is assumed that the quantities are nondimensionalized using the velocity U_0 and distance H and the boundary conditions are $u(x, 0, z, t) = u(x, b, z, t) = v(x, b, z, t) = w(x, 0, z, t) = w(x, b, z, t) = 0$. Our choice of control variable is taken to be $v(x, 0, z, t)$, which corresponds to wall-normal blowing and suction.

Introducing the wall-normal vorticity

$$\zeta(x, y, z, t) \triangleq \frac{\partial u}{\partial z} - \frac{\partial w}{\partial x} \tag{27}$$

Eqs. (23)-(26) can be simplified [2] to yield equations for the wall-normal velocity v and vorticity ζ:

$$-\nabla^2 \dot{v} + \{U \frac{\partial}{\partial x} \nabla^2 - U'' \frac{\partial}{\partial x} - \nabla^2 \nabla^2 / Re\} v = 0 \tag{28}$$

$$\dot{\zeta} + U' \frac{\partial v}{\partial z} + \{U \frac{\partial}{\partial x} - \nabla^2 / Re\} \zeta = 0 \tag{29}$$

Introducing the spatial Fourier transform in the x and z directions,

$$v(x, y, z, t) = \Re e \{\hat{v}(y, t) \exp[i(\alpha x + \beta z)]\}, \tag{30}$$

$$\zeta(x, y, z, t) = \Re e \{\hat{\zeta}(y, t) \exp[i(\alpha x + \beta z)]\} \tag{31}$$

where $\hat{v}$ and $\hat{\zeta}$ are the complex amplitudes and α, β are the real wavenumbers, leads to the Orr–Sommerfeld and Squire equations [2]:

$$\begin{bmatrix} \mathcal{M}_{os} & 0 \\ 0 & \mathcal{M}_{sq} \end{bmatrix} \begin{bmatrix} \dot{\hat{v}} \\ \dot{\hat{\zeta}} \end{bmatrix} + \begin{bmatrix} \mathcal{K}_{os} & 0 \\ \mathcal{K}_c & \mathcal{K}_{sq} \end{bmatrix} \begin{bmatrix} \hat{v} \\ \hat{\zeta} \end{bmatrix} = \begin{bmatrix} 0 \\ 0 \end{bmatrix} \tag{32}$$

where

$$\mathcal{M}_{os} = -\boldsymbol{\Delta}, \quad \mathcal{M}_{sq} = \mathcal{I}, \quad \boldsymbol{\Delta} = \partial^2/\partial y^2 - \alpha^2 - \beta^2 \tag{33}$$

$$\mathcal{K}_{os} = -i\alpha U \boldsymbol{\Delta} + i\alpha U'' + \boldsymbol{\Delta\Delta}/Re \tag{34}$$

$$\mathcal{K}_c = i\beta U', \quad \mathcal{K}_{sq} = i\alpha U - \boldsymbol{\Delta}/Re \tag{35}$$

and $\mathcal{I}$ is the identity operator.

The boundary conditions are $\hat{v}_y(0, t) = \hat{\zeta}(0, t) = 0$, $\hat{v}_y(b, t) = -k\hat{v}(b, t)$ (the inviscid asymptotic), $\hat{\zeta}(b, t) = 0$, and the (real) control inputs are taken to be

$$\boldsymbol{v}(t) = [\Re e \{\hat{v}(0, t)\} \, \Im m\{\hat{v}(0, t)\}]^\mathsf{T} = [v_r(t) \, v_i(t)]^\mathsf{T} \tag{36}$$

(the vector $\boldsymbol{v}$ should not be confused with the scalar velocity components u and v; the symbol v will not be used in this paper to refer to a fluid's kinematic viscosity). We see that the control input $\boldsymbol{v}$ can ultimately be related to the wall velocity: $v(x, 0, z, t) = \Re e \{\hat{v}(0, t)\} \cos(\alpha x + \beta z) - \Im m\{\hat{v}(0, t)\} \sin(\alpha x + \beta z)$. It is noted that the control input provides additional boundary conditions for $\hat{v}(0, t)$.

3.3 Measurements

In the sequel, we will consider measurements obtainable using shear-stress measurements at the wall. Let us select the wall-normal derivative of the wall-normal vorticity: $\hat{\zeta}_y = i\beta\hat{u}_y - i\alpha\hat{w}_y$. Note that $\hat{u}_y$ and $\hat{w}_y$ are available from measurements of the shear stresses $\hat{\tau}_{xy}(y, t) = \mu(i\alpha\hat{v}(y, t) + \hat{u}_y(y, t))$ and $\hat{\tau}_{yz}(y, t) = \mu(i\beta\hat{v}(y, t) + \hat{w}_y(y, t))$ at the wall ($y = 0$). We shall define the real output in this case as $\boldsymbol{m}_{sq} = [\Re e \{\hat{\zeta}_y(0, t)\} \, \Im m\{\hat{\zeta}_y(0, t)\}]^\mathsf{T}$. This output is motivated by the fact that the wall-normal vorticity states $\hat{\zeta}$ are not observable from outputs based on $\hat{v}$ such as those introduced in [10]. One way of seeing this is by noting the structure of Eq. (32) (or its discrete equivalent developed in the next section). However, there is the potential for $\hat{v}$ and $\hat{\zeta}$ to be observable from $\boldsymbol{m}_{sq}$ when $\beta \neq 0$ which follows from the coupling exhibited by Eq. (32) (or its discrete equivalent developed in the next section) in this case.

4 Numerical example

4.1 Spatial discretization using finite elements

The spatial discretization of the Orr–Sommerfeld/Squire equations in Eq. (32) is carried out using the same procedures used in [10]: the y-domain $[0, b]$ is broken into N_e equally-sized finite elements (width ℓ) with the value of y at the nodes (element boundaries) denoted by $y_j = (j - 1)\ell$, $j = 1, \ldots, N_e + 1$ where $\ell = (b - a)/N_e$. The value of $\hat{v}$ and its derivative at the nodes are denoted by $v_j(t) = \hat{v}(y_j, t)$ and $v'_j(t) = \hat{v}_y(y_j, t)$ with similar definitions for $\zeta_j(t)$ and $\zeta'_j(t)$. Within the jth element, the following trial solutions are assumed:

$$\hat{v}(y, t) = [1 \, \hat{y} \, \hat{y}^2 \, \hat{y}^3] \begin{bmatrix} 1 & 0 & 0 & 0 \\ 0 & \ell & 0 & 0 \\ -3 & -2\ell & 3 & -\ell \\ 2 & \ell & -2 & \ell \end{bmatrix}$$
$$\times [v_j(t) \, v'_j(t) \, v_{j+1}(t) \, v'_{j+1}(t)]^\mathsf{T}$$
$$= \boldsymbol{Y}^\mathsf{T}(\hat{y}) \boldsymbol{L} \boldsymbol{q}_{os}^{(j)}(t) \tag{37}$$

and

$$\hat{\zeta}(y, t) = \boldsymbol{Y}^\mathsf{T}(\hat{y}) \boldsymbol{L} \boldsymbol{q}_{sq}^{(j)}(t),$$
$$\boldsymbol{q}_{sq}^{(j)}(t) = [\zeta_j(t) \, \zeta'_j(t) \, \zeta_{j+1}(t) \, \zeta'_{j+1}(t)]^\mathsf{T} \tag{38}$$

where $y = (j - 1 + \hat{y})\ell$ and $\hat{y}$ is a local element coordinate system with $0 \leq \hat{y} \leq 1$. This element description was used by [15] in the case of Poiseuille flow and [10] in the Blasius case.

Based on Eq. (37), the finite element description of the Orr–Sommerfeld solution is given by

$$\hat{v}(y,t) = \sum_{j=1}^{N_e} \mathbf{\Phi}_j(y) \mathbf{q}_{os}^{(j)}(t) \tag{39}$$

$$\hat{\zeta}(y,t) = \sum_{j=1}^{N_e} \mathbf{\Phi}_j(y) \mathbf{q}_{sq}^{(j)}(t) \tag{40}$$

where

$$\mathbf{\Phi}_j(y) = \begin{cases} \mathbf{Y}^{\mathsf{T}}(\hat{y})\mathbf{L}, & (j-1)\ell \le y \le j\ell \\ \mathbf{0}, & \text{otherwise.} \end{cases} \tag{41}$$

In preparation for a weak (variational) solution of the problem, we introduce variations

$$\delta\hat{v}(y,t) = \sum_{j=1}^{N_e} \mathbf{\Phi}_j(y)\delta\mathbf{q}_{os}^{(j)}(t),$$

$$\delta\hat{\zeta}(y,t) = \sum_{j=1}^{N_e} \mathbf{\Phi}_j(y)\delta\mathbf{q}_{sq}^{(j)}(t), \tag{42}$$

satisfying the boundary conditions

$$\delta\hat{v}(a,t) = \delta\hat{v}'(a,t) = 0, \quad \delta\hat{\zeta}(a,t) = \delta\hat{\zeta}(b,t) = 0 \tag{43}$$

The upper boundary condition at $y = b$ is taken to be $\hat{v}'(b,t) = -k\hat{v}(b,t)$ and $\delta\hat{v}'(b,t) = -k\delta\hat{v}(b,t)$ which correspond to the inviscid asymptotic solution of the Orr–Sommerfeld equation, $\hat{v}(y,t) \propto e^{-ky}$.

Premultiplying the Orr–Sommerfeld/Squire equation in Eq. (32) by $[\delta\hat{v} \ \ \delta\hat{\zeta}]^{\mathsf{T}}$ followed by integration by parts and substitution of Eqs. (37)–(40) yields

$$\sum_{j=1}^{N_e} \delta\mathbf{q}_{os}^{(j)\mathsf{T}}[\mathbf{M}_{os,r,j}\dot{\mathbf{q}}_{os}^{(j)} + (\mathbf{K}_{os,r,j} + \mathrm{i}\mathbf{K}_{os,i,j})\mathbf{q}_{os}^{(j)}]$$

$$+ \sum_{j=1}^{N_e} \delta\mathbf{q}_{sq}^{(j)\mathsf{T}}[\mathbf{M}_{sq,r,j}\dot{\mathbf{q}}_{sq}^{(j)} + (\mathbf{K}_{sq,r,j}$$

$$+ \mathrm{i}\mathbf{K}_{sq,i,j})\mathbf{q}_{sq}^{(j)} + \mathrm{i}\mathbf{K}_{c,i,j}\mathbf{q}_{os}^{(j)}] = 0, \tag{44}$$

where

$$\mathbf{M}_{os,r,j} = \mathbf{L}^{\mathsf{T}} \int_0^1 \left[k^2 \mathbf{Y}(\hat{y})\mathbf{Y}^{\mathsf{T}}(\hat{y}) + \frac{1}{\ell^2}\frac{\mathrm{d}}{\mathrm{d}\hat{y}}\mathbf{Y}(\hat{y})\frac{\mathrm{d}}{\mathrm{d}\hat{y}}\mathbf{Y}^{\mathsf{T}}(\hat{y}) \right] \mathrm{d}\hat{y} \, \mathbf{L}\ell$$

$$\mathbf{K}_{os,r,j} = \frac{1}{Re}\mathbf{L}^{\mathsf{T}} \int_0^1 \left[k^4 \mathbf{Y}(\hat{y})\mathbf{Y}^{\mathsf{T}}(\hat{y}) + 2k^2\frac{1}{\ell^2}\frac{\mathrm{d}}{\mathrm{d}\hat{y}}\mathbf{Y}(\hat{y})\frac{\mathrm{d}}{\mathrm{d}\hat{y}}\mathbf{Y}^{\mathsf{T}}(\hat{y}) \right.$$
$$\left. + 2\frac{1}{\ell^4}\frac{\mathrm{d}^2}{\mathrm{d}\hat{y}^2}\mathbf{Y}(\hat{y})\frac{\mathrm{d}^2}{\mathrm{d}\hat{y}^2}\mathbf{Y}^{\mathsf{T}}(\hat{y}) \right] \mathrm{d}\hat{y} \, \mathbf{L}\ell$$

$$\mathbf{K}_{os,i,j} = \alpha\mathbf{L}^{\mathsf{T}} \int_0^1 \left\{ [(k^2 U((j-1+\hat{y})\ell) \right.$$
$$+ U''((j-1+\hat{y})\ell)]\mathbf{Y}(\hat{y})\mathbf{Y}^{\mathsf{T}}(\hat{y})$$
$$+ U((j-1+\hat{y})\ell)\frac{1}{\ell^2}\frac{\mathrm{d}}{\mathrm{d}\hat{y}}\mathbf{Y}(\hat{y})\frac{\mathrm{d}}{\mathrm{d}\hat{y}}\mathbf{Y}^{\mathsf{T}}(\hat{y})$$
$$\left. + \frac{1}{\ell}U'((j-1+\hat{y})\ell)\mathbf{Y}(\hat{y})\frac{\mathrm{d}}{\mathrm{d}\hat{y}}\mathbf{Y}^{\mathsf{T}}(\hat{y}) \right\} \mathrm{d}\hat{y} \, \mathbf{L}\ell$$

$$\mathbf{M}_{sq,r,j} = \mathbf{L}^{\mathsf{T}} \int_0^1 \left[\mathbf{Y}(\hat{y})\mathbf{Y}^{\mathsf{T}}(\hat{y}) \right] \mathrm{d}\hat{y} \, \mathbf{L}\ell$$

$$\mathbf{K}_{c,i,j} = \beta\mathbf{L}^{\mathsf{T}} \int_0^1 \left[U'((j-1+\hat{y})\ell)\mathbf{Y}(\hat{y})\mathbf{Y}^{\mathsf{T}}(\hat{y}) \right] \mathrm{d}\hat{y} \, \mathbf{L}\ell$$

$$\mathbf{K}_{sq,r,j} = \frac{1}{Re}\mathbf{L}^{\mathsf{T}} \int_0^1 \left[k^2 \mathbf{Y}(\hat{y})\mathbf{Y}^{\mathsf{T}}(\hat{y}) + \frac{1}{\ell^2}\frac{\mathrm{d}}{\mathrm{d}\hat{y}}\mathbf{Y}(\hat{y})\frac{\mathrm{d}}{\mathrm{d}\hat{y}}\mathbf{Y}^{\mathsf{T}}(\hat{y}) \right] \mathrm{d}\hat{y} \, \mathbf{L}\ell$$

$$\mathbf{K}_{sq,i,j} = \alpha\mathbf{L}^{\mathsf{T}} \int_0^1 \left[U((j-1+\hat{y})\ell)\mathbf{Y}(\hat{y})\mathbf{Y}^{\mathsf{T}}(\hat{y}) \right] \mathrm{d}\hat{y} \, \mathbf{L}\ell$$

Note that when the integration by parts yields terms evaluated at $y = b$, additional terms accrue in the matrices $\mathbf{M}_{os,r,N_e}$, $\mathbf{K}_{os,r,N_e}$, and $\mathbf{K}_{os,i,N_e}$.

Defining $\widehat{\mathbf{q}}_{os} = [v_1 \ v_1' \cdots v_{N_e+1} \ v_{N_e+1}']^{\mathsf{T}}$, $\widehat{\mathbf{q}}_{sq} = [\zeta_1 \ \zeta_1' \cdots \zeta_{N_e+1} \ \zeta_{N_e+1}']^{\mathsf{T}}$, and $\widehat{\mathbf{q}} = [\widehat{\mathbf{q}}_{os}^{\mathsf{T}} \ \widehat{\mathbf{q}}_{sq}^{\mathsf{T}}]^{\mathsf{T}}$, with the corresponding definition for $\delta\widehat{\mathbf{q}}$, Eq. (44) can be written as

$$\delta\widehat{\mathbf{q}}^{\mathsf{T}}[\widehat{\mathbf{M}}_r\dot{\widehat{\mathbf{q}}} + (\widehat{\mathbf{K}}_r + \mathrm{i}\widehat{\mathbf{K}}_i)\widehat{\mathbf{q}}] = \mathbf{0} \tag{45}$$

where the global matrices $\widehat{\mathbf{M}}_r$, $\widehat{\mathbf{K}}_r$, and $\widehat{\mathbf{K}}_i$, are formed using the usual assembly procedures of the finite element method and can be partitioned as

$$\widehat{\mathbf{M}}_r = \begin{bmatrix} \widehat{\mathbf{M}}_{os,r} & \mathbf{0} \\ \mathbf{0} & \widehat{\mathbf{M}}_{sq,r} \end{bmatrix}, \ \widehat{\mathbf{K}}_r = \begin{bmatrix} \widehat{\mathbf{K}}_{os,r} & \mathbf{0} \\ \mathbf{0} & \widehat{\mathbf{K}}_{sq,r} \end{bmatrix},$$

$$\widehat{\mathbf{K}}_i = \begin{bmatrix} \widehat{\mathbf{K}}_{os,i} & \mathbf{0} \\ \widehat{\mathbf{K}}_{c,i} & \widehat{\mathbf{K}}_{sq,i} \end{bmatrix} \tag{46}$$

Since the left-hand side of Eq. (45) must vanish for all variations $\delta\widehat{\mathbf{q}}$, we arrive at

$$\widehat{\mathbf{M}}_r\dot{\widehat{\mathbf{q}}} + (\widehat{\mathbf{K}}_r + \mathrm{i}\widehat{\mathbf{K}}_i)\widehat{\mathbf{q}} = \mathbf{0} \tag{47}$$

and we momentarily ignore the rows corresponding to $\delta q_j = 0$.

The boundary conditions are now applied by setting $v_1' = \zeta_1 = \zeta_{N_e+1} = 0$ and taking the terms involving v_1 to the right-hand side of the equation to form the control input. We also set $v_{N_e+1}' = -kv_{N_e+1}$. Defining $\mathbf{q}_{os} =$

$[v_2 \ v_2' \cdots v_{N_e} \ v_{N_e}' v_{N_e+1}]^{\mathsf{T}}$, $q_{sq} = [\zeta_1' \ \zeta_2 \ \zeta_2' \cdots \zeta_{N_e} \ \zeta_{N_e}' \ \zeta_{N_e+1}']^{\mathsf{T}}$, $q = [q_{os}^{\mathsf{T}} \ q_{sq}^{\mathsf{T}}]^{\mathsf{T}}$ and removing the appropriate rows and columns from the above equation yields

$$M_r \dot{q} + (K_r + iK_i)q = (B_{1r} + iB_{1i})v_1 + B_{2r}\dot{v}_1 \qquad (48)$$

where M_r, K_r, and K_i are the reduced matrices which can be partitioned analogous to those in Eq. (46). Additional terms are added to the last row and last column of each Orr–Sommerfeld matrix on the left-hand side to enforce $v_{N_e+1}' = -kv_{N_e+1}$. It is straightforward to form B_{1r} from the entries of $\widehat{K}_{os,r}$, B_{1i} from the entries of $\widehat{K}_{os,i}$ and $\widehat{K}_{c,i}$, and B_{2r} from the entries of $\widehat{M}_{os,r}$.

Defining $q_{os} = [v_2 \ v_2' \cdots v_{N_e} \ v_{N_e}' v_{N_e+1}]^{\mathsf{T}}$, $q_{sq} = [\zeta_1' \ \zeta_2 \ \zeta_2' \cdots \zeta_{N_e} \ \zeta_{N_e}' \zeta_{N_e+1}']^{\mathsf{T}}$, $q = [q_{os}^{\mathsf{T}} \ q_{sq}^{\mathsf{T}}]^{\mathsf{T}}$, we can define the (real) state vector to be $\widehat{x} = [q_{os,r}^{\mathsf{T}} \ q_{os,i}^{\mathsf{T}} \ q_{sq,r}^{\mathsf{T}} \ q_{sq,i}^{\mathsf{T}}]^{\mathsf{T}}$, where $q_{os,r} = \Re\mathrm{e}\,\{q_{os}\}$, $q_{os,i} = \Im\mathrm{m}\{q_{os}\}$, $q_{sq,r} = \Re\mathrm{e}\,\{q_{sq}\}$, $q_{sq,i} = \Im\mathrm{m}\{q_{sq}\}$. Defining the control input to be $v = [\Re\mathrm{e}\,\{v_1\} \ \Im\mathrm{m}\{v_1\}]^{\mathsf{T}}$, the state-space model can be written as

$$\dot{\widehat{x}} = A\widehat{x} + \widehat{B}_1 v + \widehat{B}_2 \dot{v} \qquad (49)$$

$$m = C\widehat{x} + \widehat{D}v \qquad (50)$$

If the (real) outputs are taken to be $m(t) = m_{sq}(t) = [\Re\mathrm{e}\,\{\hat{\zeta}_y(a,t)\} \ \Im\mathrm{m}\{\hat{\zeta}_y(a,t)\}]^{\mathsf{T}}$ then C contains all zeros with the exception of two entries equal to unity and $\widehat{D} = 0$.

The term containing $\dot{v}$ can be removed by defining a new state vector $x = \widehat{x} - \widehat{B}_2 v$. The ensuing state description is

$$\dot{x} = Ax + Bv, \quad B = \widehat{B}_1 + A\widehat{B}_2 \qquad (51)$$

$$m = Cx + Dv, \quad D = \widehat{D} + C\widehat{B}_2. \qquad (52)$$

If x is partitioned as $x = \mathrm{col}\{x_{os}, x_{sq}\}$, then the above matrices can be partitioned as

$$A = \begin{bmatrix} A_{os} & 0 \\ A_c & A_{sq} \end{bmatrix}, B = \begin{bmatrix} B_{os} \\ B_{sq} \end{bmatrix}, C = [C_{os} \ C_{sq}] \qquad (53)$$
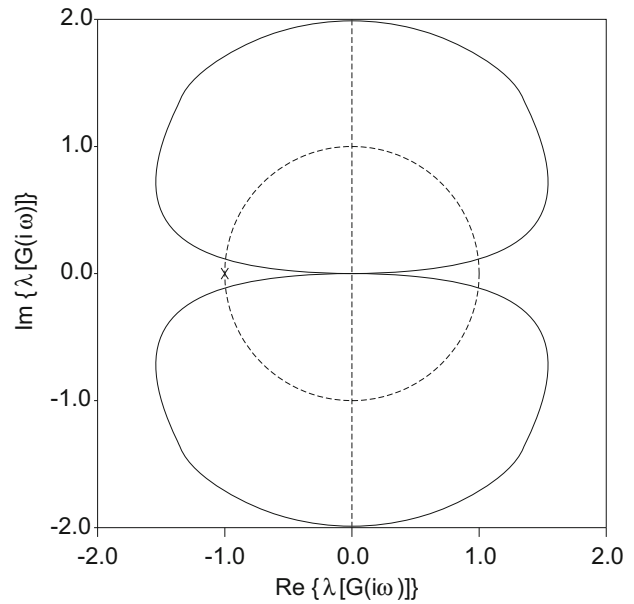

Fig. 4 Nyquist plot ($m = m_{sq}$, $Re = 1000$, $\alpha = 0$, $\beta = 0.65$)

where $C_{os} = 0$ if $m = m_{sq}$. Hence, there is the possibility that both the Orr–Sommerfeld and Squire modes [2] are controllable using v. Also both sets of modes may be observable using the output m_{sq}.

For the numerical approach, we will take $N_e = 62$ finite elements and a computational boundary of $b = 24$. The value of N_e has been selected to address two competing concerns. The first of these is to limit the number of states $n = 8N_e - 2 = 494$ to be less than 500 which is an outer limit for the desired size of the dynamic controllers which have the same number of states as the plant used for their design. The other objective was to limit the differences between the primary eigenvalues of A and the Orr–Sommerfeld/Squire eigenvalues tabulated in [2] (for $Re = 800$, $\alpha = 0.125$, and $\beta = 0.3$) to be less than 1%. This eigenvalue comparison also informed the choice of b (there is more discussion about this in [10]). The eigenvalue comparison for $N_e = 62$ and $b = 24$ is given in Table 1.

For the duration of this study, we will concentrate on the case where $Re = 1000$, $\alpha = 0$, and $\beta = 0.65$. It was shown in [4] that these wavenumbers correspond to worst case tran-

Table 1 Orr–Sommerfeld /Squire eigenvalues for Blasius case, $Re = 800$, $\alpha = 0.125$, $\beta = 0.3$

Schmid & Henningson [2]		Damaren ($N_e = 62$, $b = 24$)		Error (%)
$\Re\{\lambda/\alpha\}$	$\Im\{\lambda/\alpha\}$	$\Re\{\lambda/\alpha\}$	$\Im\{\lambda/\alpha\}$	
Orr–Sommerfeld				
−0.01526	0.4299	−0.01614	0.4301	0.21
−0.3153	0.6711	−0.3119	0.6711	0.46
−0.3663	0.4373	−0.3649	0.4374	0.25
−0.4671	0.8608	−0.4605	0.8578	0.74
Squire				
−0.1733	0.3011	−0.1733	0.3009	0.058
−0.2950	0.5308	−0.2943	0.5302	0.15
−0.3810	0.7281	−0.3795	0.7267	0.25
−0.4396	0.9163	−0.4375	0.9141	0.30

sient growth at this Reynolds number. The corresponding multivariable Nyquist plot (i.e., the eigenloci of $\boldsymbol{G}(\mathrm{i}\omega)$) is given in Fig. 4 for $\boldsymbol{m} = \boldsymbol{m}_{sq}$. The eigenvalues λ_j have been scaled to $(4/\pi)\tan^{-1}(|\lambda_j|)[\exp(\mathrm{i}\arg(\lambda_j)]$ which preserves the phase, maps zero to zero, maps the unit circle onto the unit circle, and maps ∞ onto a circle with radius two. Clearly this system is not positive real, but the system possesses an infinite gain margin.

4.2 Measuring transient growth

The worst case transient growth can be calculated as in Sect. 2.3 by taking the matrix in the energy quadratic form to be

$$\boldsymbol{Q} = \text{block diag}\{\boldsymbol{M}_{os}, \boldsymbol{M}_{os}, \boldsymbol{M}_{sq}, \boldsymbol{M}_{sq}\}. \tag{54}$$

Considering a Reynolds number of $Re = 1000$, according to [4] the maximum value of J with respect to α and β occurs at $\alpha = 0$ and $\beta = 0.65$. It was given by 1514 and the corresponding time is $T_{\max} = 778$. In our case, if $N_e = 62$ and $b = 24$ (values to be used exclusively in the sequel), the corresponding values are 1526 and 787.

4.3 Baseline case: the linear quadratic regulator (LQR)

It has been noted that the LQR case leads to state feedback which is expected to yield optimal reduction of the maximum transient growth if the weighting matrix in the LQR functional is taken to be that given in Eq. (54). The penalty on the control effort is taken to be $\boldsymbol{R} = R\boldsymbol{I}$ with $R > 0$. The values of J and the corresponding values of $T_{\max}$ are given in Table 2 for various values of R. This represents an ideal case since clearly all of the states cannot be measured. It is interesting to note that as R is reduced the transient growth asymptotes to a lower value of 221 which should be compared with the open-loop value of 1526. In Table 2, we have

Table 2 Optimal transient energy growth for the linear quadratic regulator

R	J	$T_{\max}$	$\bar{\sigma}[\boldsymbol{S}(0)]$
∞	1526	787	1
10^4	528	523	0.47
10^3	236	443	0.17
10^2	227	369	0.054
10^1	223	367	0.017
1	222	369	0.0054
0.1	221	370	0.0017
0.01	221	370	0.00054

Table 3 Optimal transient energy growth for static output feedback

$K(s)$	$\hat{\zeta}_y$ output	
	J	$T_{\max}$
0	1526	787
0.001	1523	786
0.01	1318	690
0.1	814	597
1.0	800	599
10.0	800	599
100.0	800	599

also tabulated $\bar{\sigma}[\boldsymbol{S}(0)]$ which will be used as a performance measure throughout this section.

4.4 Constant output feedback

Given the infinite gain margin for the outputs under consideration, $\boldsymbol{m}_{sq}$, it is of interest to examine the transient growth using simple static output feedback, i.e., $\boldsymbol{K}(s) = \bar{K}\boldsymbol{I}$. The corresponding values of J and $T_{\max}$ are given in Table 3 for various values of $\bar{K}$. When the wall-normal derivative of the wall-normal vorticity is used as the output ($\boldsymbol{m}_{sq}$), there is reduction of J as K increases with an asymptotic least value of 800.

Table 4 Optimal transient energy growth for the LQG/LTR controller ($R = 0.01$)

q_0	J	$T_{\max}$	$\bar{\sigma}[S(0)]$
0.01	1262	650	0.56
0.1	824	598	0.022
1	801	599	0.0011
10	801	599	0.00057
100	801	599	0.00054

Table 5 Optimal transient energy growth for the H_∞ loopshaping controller ($\gamma = 2$)

W	J	$T_{\max}$	$\bar{\sigma}[S(0)]$	$b_{G,K}$
1	811	600	0.013	0.568
10	801	599	0.0013	0.151
25	800	599	0.00053	0.0604
100	800	599	0.00013	0.015
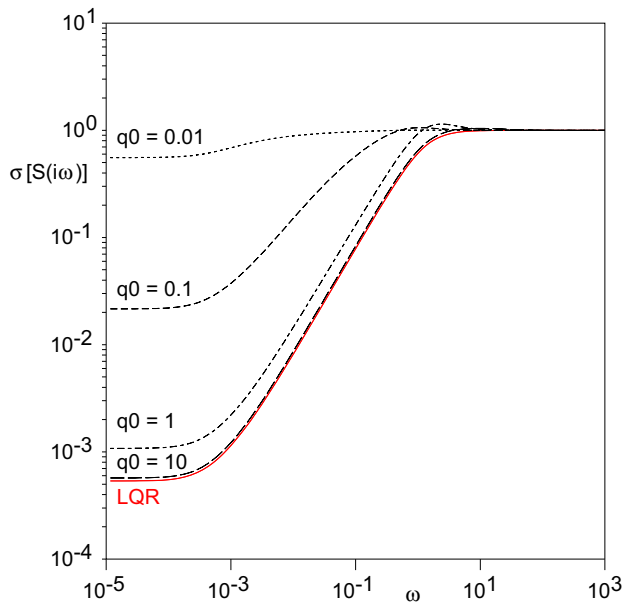
Fig. 5 Singular values of the sensitivity function vs. frequency (LQG/LTR controller)

4.5 Loop transfer recovery

Given the reduction in transient energy growth obtained using the LQR feedback, we endeavor to recover that performance using the LQG/LTR solution presented in Sect. 2.5. For the design case, the LQR weights are taken to be $R = 0.01$ and Q is selected according to Eq. (54). The singular values of the sensitivity function $S(i\omega)$ are depicted in Fig. 5 for various values of q_0 and the LQR case. It is clear that as $q_0 \to \infty$, the LQR sensitivity function is recovered as expected. An interesting question that arises is how much of the transient energy growth reduction created by the LQR controller can be recovered? The value of J is given in Table 4 for various values of q_0. Clearly convergence is achieved as q_0 is increased but the converged value is somewhat higher than the LQR value. Note that J is computed using the composite system matrix, $\bar{A}$ in the closed-loop system of Eq. (7) and the initial values of the controller states are taken to be zero when calculating the supremum with respect to the initial states. It is interesting that the converged value of J (801) is very nearly the same as that obtained using static output feedback in Table 3.

4.6 H_∞ loop shaping

We initially consider the controller yielding optimal robustness as given in Sect. 2.6 (Eqs. (14)-(15)) and corresponding to an unshaped plant, i.e., $W(s) = I$. The minimum value of $||[G(s), K(s)]||_\infty$ is $\gamma_{\min} = 1.347$ which yields an optimal robustness level of $b_{opt} = \gamma_{\min}^{-1} = 0.742$. The closer the chosen value of γ used in Eqs. (14)-(15) is to $\gamma_{\min}$, the closer the closed-loop system will be to optimal robustness. By increasing the distance between the chosen value of γ and $\gamma_{\min}$, one can increase performance at the expense of robustness. A value of $\gamma = 2$ was selected which yielded a value of $||[G(s), K(s)]||_\infty = 1.761$, hence $b_{G,K} = 0.568$, and a DC sensitivity of 0.013 occurs (see Table 5). The transient energy growth is $J = 811$.

As the loop-shaping weight W is increased there is an increase in performance as measured by the sensitivity reduction and the transient growth asymptotes to a minimum value of 800. This is virtually the same at that obtained using static output feedback and an LQG/LTR controller. The best obtainable transient growth appears to be a property of the chosen output and is independent of the controllers used. The behavior of the sensitivity function is given in Fig. 6 and it is clear that increasing W leads to increasing sensitivity reduction.

4.7 Model order reduction and reduced order controller

In this section, the plant design model is reduced using the procedures of Sect. 2.9. First, a modal representation is reduced to the 100 most controllable/observable modes. Then, a reduced order model of order N_c is obtained using balanced truncation. The H_∞ loop-shaping design procedure is employed with $W = 25$ and $\gamma = 2$. The Hankel singular values are given in Table 6 and it is clear that they roll off fairly quickly. The sensitivity reduction at $\omega = 0$ and the transient growth measure J are given in Table 7 as a function of N_c. It is very interesting to note that the closed-loop behavior is relatively insensitive to N_c and a good design is obtained for $N_c = 2$. The sensitivity function is compared to the full-order design in Fig. 11; they are nearly identical. For this value, the quantity b_{G_r, K_r} (the norm of the system in Eq. (6) using the reduced order plant and controller) is 0.0608.
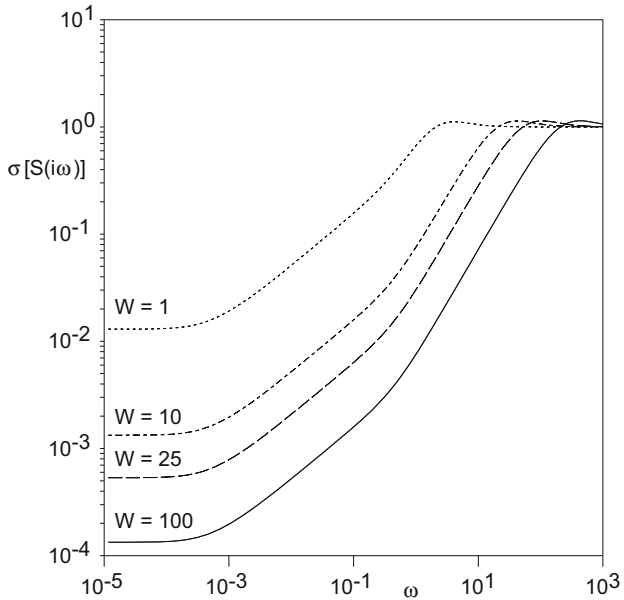
Fig. 6 Singular values of the sensitivity function vs. frequency (H_∞ loop-shaping controller)

Table 6 Hankel singular values

j	σ_j
1	2.52
2	2.52
3	0.314
4	0.314
5	0.0256
6	0.0256
7	0.00188
8	0.00188
9	9.54×10^{-5}
10	9.54×10^{-5}

Table 7 Optimal transient energy growth for the reduced order $\mathcal{H}_\infty$ loopshaping controller ($W = 25$, $\gamma = 2$)

N_c	Γ_{N_c}	J	$T_{\max}$	$\bar{\sigma}[\boldsymbol{S}(0)]$	$b_{G_r K_r}$	δ_g
2	0.6834	800	599	0.00054	0.0608	0.0518
4	0.0551	800	599	0.00054	0.0610	0.0040
6	0.0040	800	599	0.00054	0.0610	0.0037
8	0.0002	800	599	0.00054	0.0610	0.0034

The gap metric between the reduced order plant $\boldsymbol{G}_r(s)$ and the full-order model is $0.0518 < 0.0608$. Hence, the reduced order design is guaranteed to stabilize the full-order plant which is already clear from the closed-loop eigenvalues and the behavior of the sensitivity function.
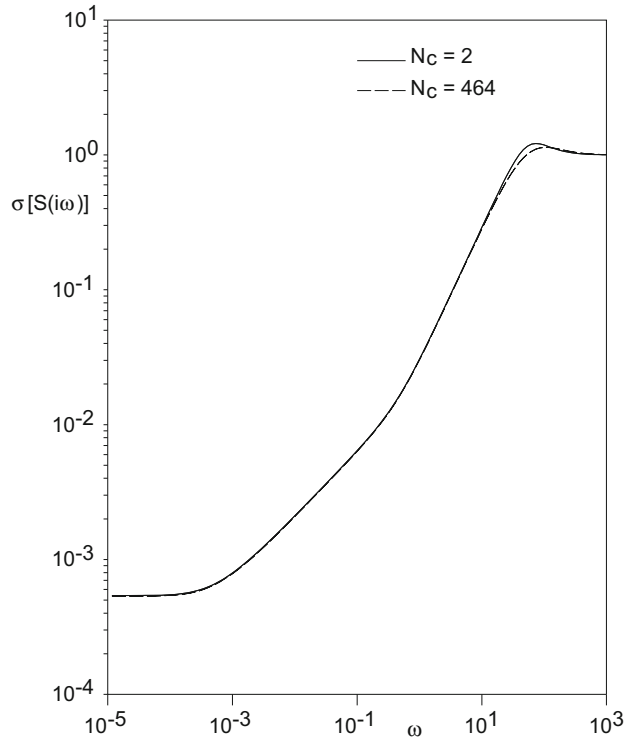

Fig. 7 Singular values of the sensitivity function vs. frequency (reduced order H_∞ loop-shaping controller)

5 Conclusions

In this paper, the methods of linear multivariable output feedback control have been applied to the problem of suppressing the transient energy growth in a Blasius boundary layer. The linearized dynamics governing perturbations of the base flow have been taken to be the usual Orr–Sommerfeld/Squire equations after spatial Fourier transforms have been used to reduce the dynamics to those governing the wall-normal velocity and the wall-normal vorticity. The control input has been taken to be the wall-normal velocity on the plate boundary. The measurements have been taken to be the first spatial derivative (wall-normal direction) of the wall-normal vorticity measured at the wall which is obtainable from shear-stress measurements on the wall. It was shown that this output is useful when combined with a wide variety of multivariable output feedback strategies. Nearly all cases led to the same value of the maximum transient energy growth. An interesting result was that the loop transfer recovery (LTR) approach allowed the sensitivity function of an LQR design to be recovered but the maximum transient energy growth (approximately 800 for LTR) could not approach the LQR value of 221.

The LQR value is independent of the sensing choice (it is state feedback) but the value for the transient growth (221) is still somewhat large. This is a strong function of the input

actuation method adopted (wall normal velocity) which suggests that other actuation mechanisms be studied with a view to reducing it. The limiting value of the transient growth (approximately 800) for the various control methods and the chosen sensor output suggests that other sensing mechanisms be studied as well.

In the Introduction, the present work was motivated by the suggestion that large transient growth of flow perturbations could induce laminar to turbulent transition by (nonlinear) mechanisms that bypassed the usual ones predicted by linear stability theory (the so-called Tollmien–Schlichting waves). The significance of our work lies in showing that the adopted actuation and sensing paradigms coupled with linear robust control theory could reduce worst case transient energy growth by close to 50% (1525 to 800). It is suggested that this reduction could lead to postponement of boundary layer transition to larger Reynolds numbers (hence, larger distances along the plate).

Declarations

Conflict of Interest The author has no relevant financial or non-financial interests to disclose.

References

1. Drazin PG, Reid WH (1981) Hydrodynamic stability. Cambridge University Press, New York. https://doi.org/10.1017/CBO9780511616938
2. Schmid PJ, Henningson DS (2001) Stability and transition in shear flows. Springer, New York. https://doi.org/10.1007/978-1-4613-0185-1
3. Schlichting H (1979) Boundary-layer theory, 7th edn. McGraw-Hill, New York
4. Butler KM, Farrell BF (1992) Three-dimensional optimal perturbations in viscous shear flow. Phys Fluids A 4(8):1637–1650. https://doi.org/10.1063/1.858386
5. Bewley TR (2001) Flow control: new challenges for a new renaissance. Prog Aerosp Sci 37:21–58. https://doi.org/10.1016/S0376-0421(00)00016-6
6. Joshi SS, Speyer JL, Kim J (1997) A systems theory approach to the feedback stabilization of infinitesimal and finite-amplitude disturbances in plane poiseuille flow. J Fluid Mech 332:157–184
7. Bewley TR, Liu S (1998) Optimal and robust control and estimation of linear paths to transition. J Fluid Mech 365:305–349. https://doi.org/10.1017/S0022112098001281
8. Bagheri S, Brandt L, Henningson DS (2009) Input-output analysis, model reduction, and control of the flat-plate boundary layer. J Fluid Mech 620:263–298. https://doi.org/10.1017/S0022112008004394
9. Belson BA, Semeraro O, Rowley CW, Henningson DS (2013) Feedback control of instabilities in the two-dimensional blasius boundary layer: the role of sensors and actuators. Phys Fluids 25:054106. https://doi.org/10.1063/1.4804390
10. Damaren CJ (2019) Transition control of the blasius boundary layer using passivity. Aerosp Syst 2(1):21–31. https://doi.org/10.1007/s42401-018-0021-0
11. Desoer CA, Vidyasagar M (1975) Feedback systems: input-output properties. Academic Press, New York. https://doi.org/10.1137/1.9780898719055.ch6
12. Damaren CJ (2016) Laminar-turbulent transition control using passivity analysis of the orr-sommerfeld equation. J Guid Contr Dyn 39(7):1602–1613. https://doi.org/10.2514/1.G001763
13. Sharma AS, Morrison JF, McKeon BJ, Limbeer DJN, Koberg WH, Kerwin SJ (2011) Relaminarisation of ReT=100 globally stabilising linear feedback control. Phys Fluids 23:125105. https://doi.org/10.1063/1.3662449
14. Heins PH, Jones BL, Sharma AS (2016) Passivity-based output-feedback control of turbulent channel flow. Automatica 69:348–355. https://doi.org/10.1016/j.automatica.2016.03.007
15. Mamou M, Khalid M (2004) Finite element solution of the orr-sommerfeld equation using high precision hermite elements: plane poiseuille flow. Int J for Num Meth Fluids 44:721–735. https://doi.org/10.1002/fld.661
16. Zames G, El-Sakkary A (1980) Unstable systems and feedback: the gap metric. In: Proceedings of the allerton conference, pp 380–385
17. Georgiou TT, Smith MC (1990) Optimal robustness in the gap metric. IEEE Trans Autom Control 35(6):673–685. https://doi.org/10.2514/1.46479
18. Jones BL, Heins PH, Kerrigan EC, Morrison JF, Sharma AS (2015) Modelling for robust feedback control of fluid flows. J Fluid Mech 769:687–722. https://doi.org/10.1017/jfm.2015.84
19. Gibeau B, Ghaemi S (2022) Laminar boundary layer forcing with active surface deformations. Phys Rev Fluids 7:114101. https://doi.org/10.1103/PhysRevFluids.7.114101
20. Methel J, Forte M, Vermeersch O, Casalis G (2022) Experimental investigation on the effect of forward-facing steps and gaps combined with wall suction on boundary layer transition. Exp Fluids 63(3):21. https://doi.org/10.1007/s00348-021-03361-x
21. Li Y, Chen Z (2021) Feedback control of boundary layer tollmien-schlichting waves using a simple model-based controller. Chin J Aeronaut 34(3):25–38. https://doi.org/10.1016/j.cja.2020.08.038
22. Gluzman I, Gayme DF (2021) Input-output framework for actuated boundary layers. Phys Rev Fluids 6:053901. https://doi.org/10.1103/PhysRevFluids.6.053901
23. Svorcan J, Wang JM, Griffin KP (2022) Current state and future trends in boundary layer control on lifting surfaces. Adv Mech Eng 14(7):1–23. https://doi.org/10.1177/16878132221112161
24. O'Connor J, Diessner M, Wilson K, Whalley RD, Wynn A, Laizet S (2023) Optimisation and analysis of streamwise-varying wall-normal blowing in a turbulent boundary layer. Flow Turb Combustion 110(3):993–1021. https://doi.org/10.1007/s10494-023-00408-3
25. Vidyasagar M (1992) Nonlinear control systems, 2nd edn. Prentice-Hall Inc, Upper Saddle River, NJ

26. Farrell BF (1988) Optimal excitation of perturbations in viscous shear flows. Phys Fluids 31(8):2093–2102. https://doi.org/10.1063/1.866609

27. Doyle JC, Stein G (1981) Multivariable feedback design: concepts for a classical/modern synthesis. IEEE Trans Autom Control 26(1):4–16. https://doi.org/10.1109/tac.1981.1102555

28. Glover K, McFarlane D (1989) Robust stabilization of normalized coprime factor plant descriptions with h_∞-bounded uncertainty. IEEE Trans Autom control 34(8):821–830. https://doi.org/10.1016/0021-9991(77)90102-4

29. Vidyasagar M (1988) Normalized coprime factorizations for non-strictly proper systems. IEEE Trans Autom Control 33(3):300–301. https://doi.org/10.1063/1.1693363

30. Georgiou TT (1988) On the computation of the gap metric. Syst Control Lett 11(4):253–257. https://doi.org/10.1109/tct.1959.1086518

31. Green M, Glover K, Limebeer D, Doyle J (1990) A j-spectral factorization approach to h_∞ control. SIAM J Control Optim 28(6):1350–1371. https://doi.org/10.1137/0328071

32. McFarlane D, Glover K (1992) A loop shaping design procedure using h_∞ synthesis. IEEE Trans Autom Control 37(6):759–769. https://doi.org/10.1016/0021-9991(77)90102-4

33. Moore BC (1981) Principal component analysis in linear systems: controllability, observability and model reduction. IEEE Trans Autom Control 26(1):17–32. https://doi.org/10.1109/tac.1981.1102568

34. Glover K (1984) All optimal hankel-norm approximations of linear multivariable systems and their l^∞- error bounds. Int J Control 39(6):1115–1193. https://doi.org/10.1080/0020718408933239